OCEANOGRAPHY

Rapid observations of ocean dynamics and stratification along a steep island coast during Hurricane María

Olivia M. Cheriton[1]*, Curt D. Storlazzi[1], Kurt J. Rosenberger[1], Clark E. Sherman[2], Wilford E. Schmidt[2]

Hurricanes are extreme storms that affect coastal communities, but the linkages between hurricane forcing and ocean dynamics remain poorly understood. Here, we present full water column observations at unprecedented resolution from the southwest Puerto Rico insular shelf and slope during Hurricane María, representing a rare set of high-frequency, subsurface, oceanographic observations collected along an island margin during a hurricane. The shelf geometry and orientation relative to the storm acted to stabilize and strengthen stratification. This maintained elevated sea-surface temperatures (SSTs) throughout the storm and led to an estimated 65% greater potential hurricane intensity contribution at this site before eye passage. Coastal cooling did not occur until 11 hours after the eye passage. Our findings present a new framework for how hurricane interaction with insular island margins may generate baroclinic processes that maintain elevated SSTs, thus potentially providing increased energy for the storm.

INTRODUCTION

Tropical cyclones (TCs), also known as typhoons and hurricanes, are extreme storms that can produce destructive winds, high storm surges, torrential rains, and flooding. When TCs affect populated coastlines, the result is usually tremendous damage to property and loss of life, making them one of the most feared and destructive weather systems on Earth. While TC intensity forecasts have improved over the past few decades (*1*), improvements in the 24- to 48-hour warning window have lagged, and the prediction skill for TC rapid intensification (RI) is still poor (*2*, *3*). Accurate forecasts of RI or deintensification for landfalling TCs remain a critical challenge but are imperative for protecting coastal communities (*4*).

The ocean response can exert strong feedbacks in TC forcing because sea-surface temperatures (SSTs) are a primary factor controlling the energy available to TCs (*5*–*7*). Strong wind and large waves can act to entrain cooler waters from depth, driving a decrease in SSTs under TCs, with the magnitude of this cooling dependent on mixed layer depth and vertical stratification (*8*–*11*). This can result in a negative feedback, whereby cooler SSTs decrease the enthalpy flux from the ocean to the atmosphere, resulting in reduced storm intensity. However, observed SST cooling does not increase monotonically with increasing TC intensity (*12*), and there is evidence that in coastal waters over narrow continental shelves upper-ocean cooling can be negligible (*13*).

In proximity to coastal boundaries, the ocean response to TC forcing is not well understood due to both a paucity of in situ observations and models lacking sufficient resolution and complexity. The few full water column observations of TC-forced ocean dynamics along coasts predominantly come from broad continental shelves, such as the Mid-Atlantic Bight (*14*–*16*) or the Gulf of Mexico (*17*–*19*). Along broad shelves, the interaction of TC winds and coastal stratification with a land barrier can either increase SST cooling through strong shear- and bottom-friction induced mixing (*14*, *15*, *17*, *18*) or limit SST cooling through downwelling (*16*, *20*, *21*). However, it is unclear if these dynamics translate to the steep, narrow, insular shelves of islands, which are disproportionately affected by TC storms. The few direct in situ measurements taken along steep island margins during TC conditions reveal several post-eye coastal dynamics: the alongshore advection of TC-upwelled waters (*22*), wind-driven cooling over shallow reef flats (*22*), as well as strong near- and subinertial baroclinic responses, such as coastally trapped waves (*23*). These previous observations report on coastal island dynamics driven by alongshore TC winds. To our knowledge, this is the first set of observations from an insular shelf to report dynamics (i) at these fine temporal (subminute) and vertical (<5 m) scales and (ii) driven by cross-shore TC winds.

Hurricane María, the strongest weather system to affect Puerto Rico since 1928, caused thousands of deaths (*24*), more than $90 billion in damage (*25*), and the largest electrical blackout in U.S. history (*26*). During María, an array of oceanographic sensors were deployed off the southwest coast of Puerto Rico as part of a months-long experiment to investigate wave and circulation dynamics on the southern insular shelf and steep upper slope (Fig. 1). Here, the insular shelf extends 5 to 10 km offshore to the shelf break at ~20-m depth, below which the upper slope (20- to 90-m depths) ranges from 25° to 45°, with a gradient of approximately 44° at our slope site (*27*). The array included nearshore pressure sensors, an outer shelf waves and current profiler, an upper slope current profiler, and thermistor moorings at the shelf break and upper slope (see Materials and Methods). The resulting dataset provides a unique opportunity to examine the hydrodynamics and baroclinic processes under TC forcing at an unprecedented temporal and vertical scale and also represents one of the first full water column observations of TC-driven coastal processes over a steep island margin.

RESULTS

Wind and wave forcing during Hurricane María

Hurricane María made landfall on the southeast corner of Puerto Rico at ~10:15 on 20 September 2017 (note: all times in GMT), and the eye passed over the longitude of buoy 42085, as marked by a sudden

[1]Pacific Coastal and Marine Science Center, U.S. Geological Survey, 2885 Mission Street, Santa Cruz, CA 95060, USA. [2]Department of Marine Sciences, University of Puerto Rico-Mayagüez, P.O. Box 9000, Mayagüez, PR 00681, Puerto Rico.
*Corresponding author. Email: ocheriton@usgs.gov

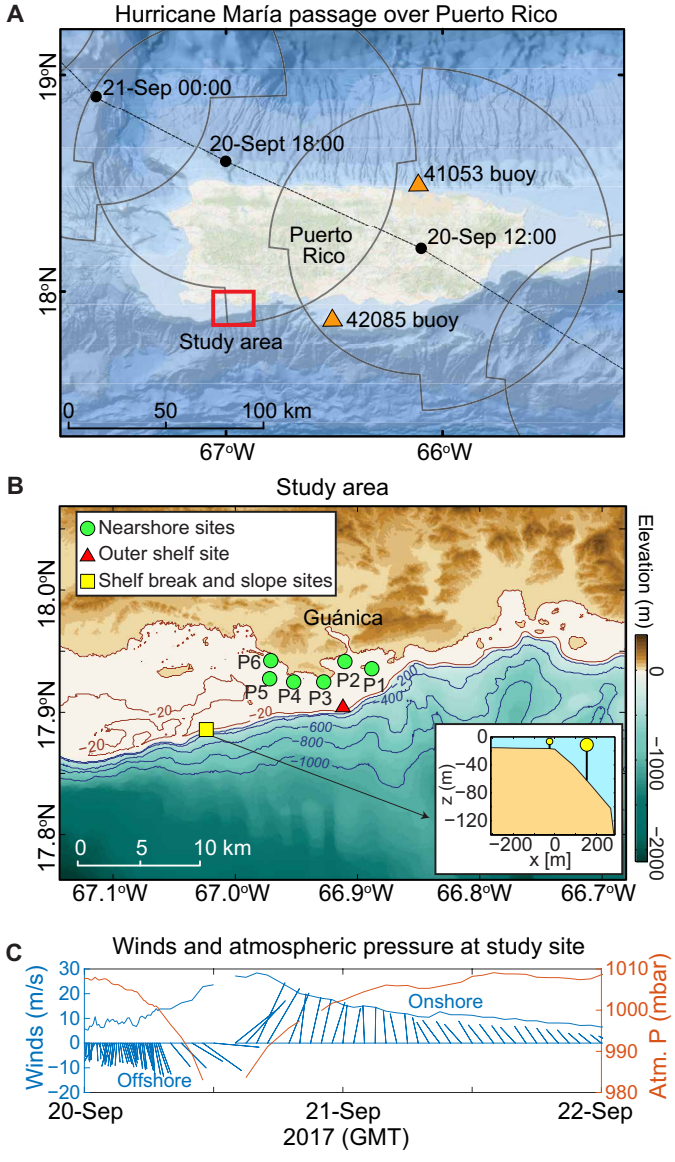

Fig. 1. Overview of the study area and the passage of Hurricane María. (**A**) Map of Puerto Rico showing study area location (red box), the oceanographic buoys (orange triangles), and the track of María with eye timing and locations (black dots) in 6-hour increments and the wind radii of 64-knot winds (gray circular outlines). (**B**) Study area showing location of nearshore shelf instrument packages (P1 to P6), the outer shelf wave and current meter (red triangle), as well as the shelf break mooring and the upper slope mooring and current meter (yellow square). Inset box shows approximate bathymetric profile of upper slope and across-shore location of shelf break and slope sites according to distance offshore of the shelf break. (**C**) Wind velocity (blue) and atmospheric pressure (orange) measured at buoy 42085 during hurricane passage. Stick vector directions point in "direction toward."

wind reversal, at 13:00. Given path and speed of Maria across Puerto Rico from the National Hurricane Center best track record, we estimate that this wind reversal occurred approximately 5 hours later at our study site (Fig. 1C), which we hereafter refer to as the eye passage. Winds at buoy 42085 exceeded 25 m s^{-1}, with gusts of 35 m s^{-1}. During the eye passage, wave periods increased from ~12 to 19 s, significant wave heights increased from 2.6 to 3.8 m, and maximum wave heights nearly doubled from ~3.8 to 7.3 m (fig. S1, A and B). In the week preceding María (13 to 20 September), the warm surface mixed layer over the upper insular slope was between 35 and 50 m deep; 10 hours before the storm (00:00 to 10:00 on 20 September), the surface mixed layer was approximately 35 m deep and moving northwestward (Fig. 2, A and C).

Wind-driven flow and thermal structure

During the initial phase of María, the northwesterly winds accelerated, and the upper currents over the shelf and slope (surface to ~35-m depth) were predominantly aligned with the accelerating northwesterly winds, with a southeastward (off-shelf) direction (Fig. 2, B and C). As the off-shelf–directed surface flow layer strengthened, the surface mixed layer (delineated by the 29.5°C isotherm) shoaled 20 m in approximately 2.5 hours (from 07:30 to 10:00 on 20 September) with increasingly cooler temperatures infiltrating at depth (Fig. 2A). The shoaling isotherms exhibited extensional (diverging) strain and were associated with weakly upward flow (~07:30 to 15:00 on 20 September; fig. S1, C and D); however, we note that the upward flow was close to the error for the instrument (~0.8 cm s^{-1}). Approximately 4 hours before the eye passage (14:00 on 20 September), the thermocline deepened to below the shelf break depth (~20 m), where the upward movement of the isotherms remained impeded by the vigorous eastward and off-shelf surface flow, which reached maximum current speeds exceeding 0.8 m s^{-1} around the time of the eye passage (18:00 on 20 September). With the arrest of the thermocline at the shelf break, cooler water continued to infiltrate at depth, causing the thermocline to further strengthen. Below the surface flow, at approximately 15:00 on 20 September, a strong shear layer developed, which became colocated with the thermocline (Fig. 2D and fig. S1F). Within this thin shear layer, there was an onshore flow (Fig. 2C), which was likely a return flow formed in direct response to the off-shelf surface flow, as the off-shelf flux within the surface layer was moderately negatively correlated with the onshore flux within the shear layer (correlation coefficient = −0.5, $P < 0.005$, degrees of freedom = 442; fig. S1H).

The water column structure was remarkably stable throughout the passage of María. Throughout the period of maximum wind and wave forcing, the strong, shallow thermocline persisted and strengthened (Fig. 2D). No expansive regions of shear instabilities ($Ri_g < 0.25$), elevated turbulent kinetic energy (TKE) dissipation ($\varepsilon > 10^{-6}$ W kg^{-1}), or large overturns ($L_T > 10$ m) were detected within or below the thermocline during this period (Fig. 2E and fig. S1E), indicating a lack of turbulence and mixing despite the strong storm energetics. Using the wave-amplitude–based Reynolds number (*28*), the time period over which the waves at our study site could produce turbulent motions and effectively deepen the mixed layer was found to be 8 hours before to 4 hours after the eye passage (10:00 to 22:00 on 20 September). Previous observations of mixed layer deepening due to TC waves found a mean mixed-layer deepening rate of 0.7 mm s^{-1} (*29*). Applying this rate, the wave-induced mixed layer depth would have reached the seabed at our slope site (60-m depth) by the time of eye passage. This was not observed; instead, the thermocline shoaled during period of large waves. We propose that the surface mixed layer remained shallow because of the wind-driven baroclinic response at the shelf break, which effectively impeded the generation of turbulence and mixing in the lower water column.

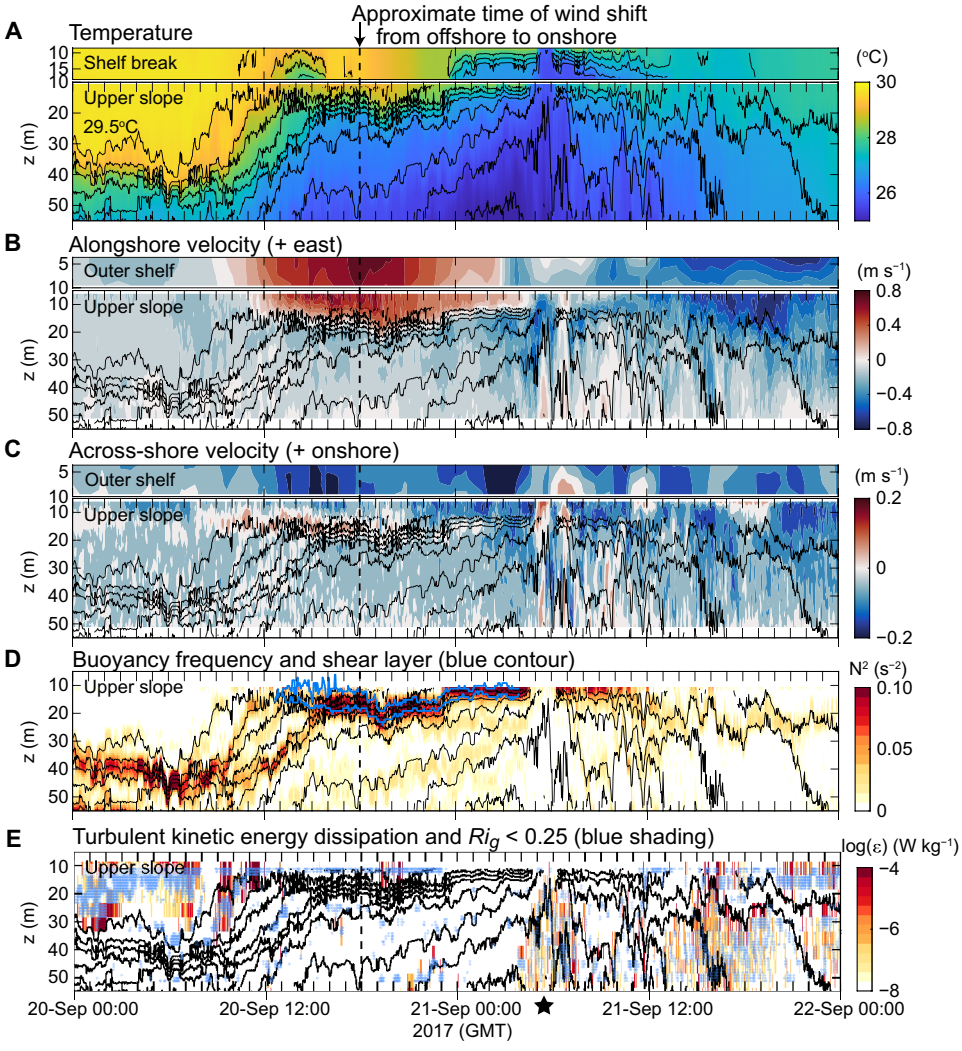

Fig. 2. Two-day time series of flow and water column response at the shelf break, outer shelf, and upper slope during Hurricane María. (**A**) Temperature (please note that the thermistor moorings overlap vertically); (**B**) alongshore current velocity; (**C**) across-shore current velocity; (**D**) buoyancy frequency squared with shear layer outlined in blue; (**E**) TKE dissipation with regions of shear instabilities (Ri_g < 0.25) shown in light blue, and the star indicates start of cold wake impact. For all panels, isotherms in 0.5°C increments (from 25° to 30°C) are shown, and the vertical dashed line indicates the approximate timing of eye passage at the study site and the shift from offshore to onshore winds [approximately 18:00 on 20 September (GMT)]. For (A) to (C), the top panels are from the outer shelf (Fig. 1B, red triangle) and shelf break sites (Fig. 1B, yellow square, 18-m depth) and the bottom panels are from the upper slope site (Fig. 1B, yellow square, 55-m depth). The *x*-axis tick marks are in hourly increments.

Impact of trailing cold wake

In the previous section, we described the ocean response during the strongest wind and wave forcing, which resulted in sustained, elevated SST throughout the storm. Here, we will detail the post-storm arrival of the cold wake, the impact of which at the steep shelf break generated a superinertial surface longwave and a subsurface, cold, bore-like internal wave.

The thermocline remained within our vertical depth coverage (as shallow as 9-m depth) until approximately 10 hours after the eye passage when there was a sudden energetic adjustment of the water column. This adjustment or internal "shock" was characterized by exceptionally cool and near-uniform temperatures throughout the water column, a rapid reversal of currents, large overturns (L_T > 10 m), and mixing (marked by star in Fig. 2 and fig. S1E). We attribute this internal shock to the relaxation in the wind-forced baroclinic dynamics and the hurricane wake's first upwelling cycle affecting the upper insular slope. The along-track internal structure of a hurricane wake is characterized by alternating cells of upwelling and downwelling (*30*) with corresponding velocity fluctuations (*31*). Estimating the distance of the wake behind the eye as $U_h(\pi\text{-}\alpha)/f$ after (*7*), where U_h is the hurricane translation speed (~5 to 7 m s^{-1} in the 10 hours before María made landfall on Puerto Rico), α is the wind inflow angle (20 to 40°), and f is the inertial frequency (0.45 × 10^{-4} s^{-1}), gives a distance of approximately 300 km separating the hurricane eye from the upwelling wake. Given the observed time separation of 10 hours, this corresponds to a translation speed of ~8 m s^{-1} for the trailing wake, comparable to the hurricane translation speed range. Satellite SST imagery from 21 September also resolves a cool, wake-like pattern with a wavelength (spatial separation) of ~300 km (fig. S2C).

In the hour preceding the wake impact (~4:00 to 5:00 on 21 September), the upper water column horizontal velocities decelerated and shifted direction from upstream and offshore to downstream and onshore (Fig. 2, B and C, and fig. S1C). Then, with the upwelling wake impact (at ~5:05 on 21 September), the slope water column cooled rapidly, with the largest temperature decrease near the surface, resulting in a nearly uniform temperature between 9-m depth and the slope bed (Fig. 3A). Temperatures at the shelf break decreased 2.5°C in 13 min to 25.6°C, while vertical velocities shifted from downward (~0.04 m s^{-1}) to upward, reaching 0.05 m s^{-1} in the upper water column above the shelf break over a 15-min time period (Fig. 2, B and C, and fig. S1C). The wake water column was highly unstable, with reduced vertical structure (mean N^2 ~ 0.002 s^{-2}), evidence of shear instabilities (Ri_g < 0.25), elevated TKE dissipation, and overturns of 10 to 20 m (Fig. 2, D and E, and fig. S1E). Within the wake, the internal Froude number (which can be used to characterize the way a flow behaves over topography, particularly at sharp interfaces such as a shelf break) increased to >0.8 in the water column above the shelf break depth, reaching a maximum of 1.0 just above the shelf break depth (fig. S1G), indicating supercritical flow conditions.

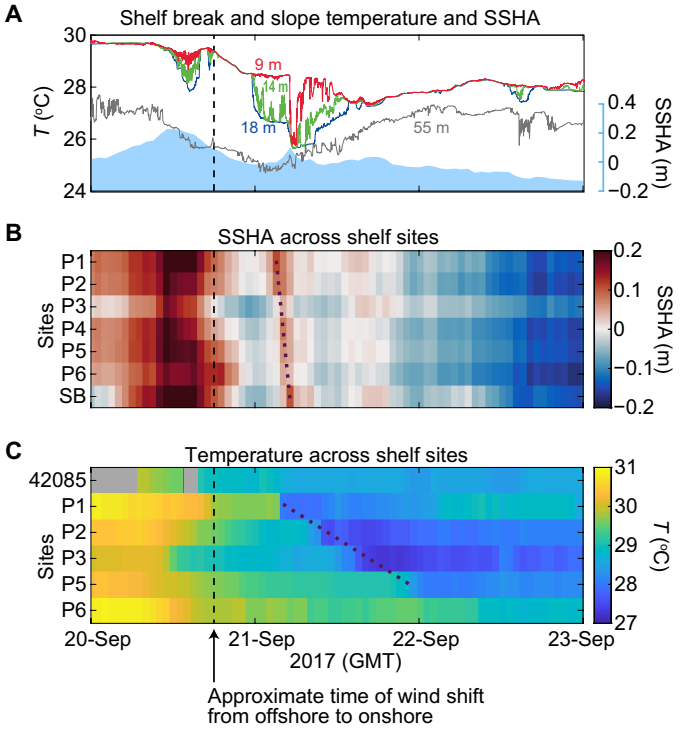

Fig. 3. Three-day time series of detided SSHAs and water temperature during Hurricane María. (**A**) Temperature at the shelf break (9-, 14-, and 18-m depth) and close to seabed on upper slope (55 m); SSHA measured at shelf break indicated by blue shading. (**B**) SSHA at nearshore shelf sites P1 to P6 and SB ordered by east-to-west alongshore position; purple dotted line represents timing and "downcoast" propagation of SSHA. (**C**) Water temperature from surface at buoy 42085 (gray = unavailable data) and near-bed temperature from nearshore shelf sites (excepting P4 due to sensor failure); purple dotted line represents timing and downcoast propagation of the cold bore-like wave. For all panels, the vertical dashed line indicates the approximate timing of eye passage at the study site and the shift from offshore to onshore winds [approximately 18:00 on 20 September (GMT)].

When the trailing cold wake affected the steep upper slope, a superinertial long wave was generated that propagated across the shelf with a period of 10 to 13 hours (the inertial period at this site is ~39 hours) and a sea-surface height anomaly (SSHA) amplitude of approximately 0.16 m at the shelf break, decaying with distance toward shore, to a minimum recorded amplitude of 0.07 m at P6 (Fig. 3, A and B). This SSHA peak appeared at all the nearshore sites in a downstream order and was distinct from the wave-driven storm surge SSHA of ~0.2 m that occurred before the eye passage. Using the timing of the SSHA peak at the shelf sites, the phase speed of this SSHA wave was estimated as 3.0 m s^{-1} heading downstream and onshore (310°) with an alongshore speed at the shelf break of approximately 2.2 m s^{-1}. The amplitude decay from the shelf break toward shore, coupled with the superinertial period and direction, suggests that this was a free wave generated by the interaction of the wake's barotropic velocity with slope topography. Before landfall on Puerto Rico, María had a mean translation speed of 5 m s^{-1} and a radius of maximum winds of approximately 200 km, corresponding to a storm time scale of 11 hours, which matches the superinertial period of this wave, further corroborating this hypothesis. The relatively short period of this wave stands in contrast to the inertial- and subinertial-period coastally trapped waves (CTWs) that were observed along the steep upper slope of Palau after the passage of Typhoon Haiyan (*23*). Storm-generated edge waves have been observed over broad continental shelves at periods similar to the wave observed here (*32*), but it is unlikely that the cross-shore bathymetric geometry (narrow insular shelf and relatively steep upper slope) could generate and support edge wave propagation.

The maximum cooling over the shelf occurred 11 to 30 hours after the passage of María and was driven by a cold, bore-like internal wave generated by the impact of the wake with the upper slope. At the shelf break, the SSHA peak coincided with the generation of this cold bore: Within 12 min, an exceptionally cold (26°C) wall of water infiltrated the lower shelf water column to at least mid-water column depths (9 m) and was observed at the shelf break for ~44 min (Fig. 3A). It subsequently propagated across the shelf, reaching all of our nearshore sites in a similar downstream order, resulting in a near-bed temperature decrease >3°C at some of the nearshore sites (compared to pre-María conditions; Fig. 3C), a cooling signature that could not have been captured by surface temperature measurements. At the shelf break, the bore phase speed estimated as $c = N_o H/\pi$ gives 0.3 m s^{-1}, while the timing of the cooling signature at the nearshore sites suggests a phase speed of 0.2 m s^{-1} with a heading the same as the SSHA wave (309°).

DISCUSSION

Potential increase in storm energy

Determining how coastal ocean processes contribute energy to landfalling TCs is critical to accurately forecasting storm intensities for coastal populations (*19*, *33*). As Hurricane María approached Puerto Rico, it underwent an RI: 48 hours before landfall, María was a Category 1 TC with 44 m s^{-1} winds, but just a few hours before landfall, it had intensified to a Category 5 with 77 m s^{-1} winds (as it made landfall, María weakened slightly to a high Category 4 due to an eyewall replacement) (*34*). Few modeling forecasts for María's intensity preceding landfall indicated RI, and none accurately captured the magnitude or timing of this RI (*34*, *35*). The potential intensity (PI) of a TC is governed by the conditions at the air-sea

interface (*36*); from the eye out to a radius of approximately 100 km (*37*), the upward enthalpy flux from the ocean surface to the atmosphere is a critical factor to storm intensity and structure (*38*).

To evaluate how the observed elevated SSTs might affect the storm energetics, we examined the increase in storm PI [(following (*36*)] that would result with no topographically forced water column stabilization at the shelf break (Fig. 4). A simple model was constructed using the pre-storm temperature profile and applying the mean, depth-variable shoaling rate of the isotherms before they reached the shelf break. The difference between the observed and modeled temperatures gives a warm anomaly of over 3°C in the surface mixed layer during the storm passage (Fig. 4D). With these anomalously warm SSTs, we estimate a mean increase in PI of 65% in the 10 hours preceding eye passage (Fig. 4E). Additional ocean temperature observations from around the island and farther offshore indicate that these anomalously warm SSTs were not confined to our immediate study area. Remotely sensed SST measurements show that SSTs extending as far as 200 km offshore (southward) from our study site were of comparable magnitude (within 0.6°C; figs. S2 and S3). Coastal buoy observations also confirm this larger-scale pattern of elevated SSTs. The SSTs from buoy 42085 (Fig. 1A) that was also located near the shelf break but approximately 40 km to the east of our study area also show sustained, warm SSTs throughout the passage of María, suggesting that the warm SSTs over the insular shelf and upper slope extended over most of the island's southern margin (fig. S4A). We also compared our results to the PI resulting from the air-sea enthalpy flux at a site on the northern insular shelf (buoy 41053; Fig. 1), which was located to the right of the TC track. This PI was of comparable magnitude to that from our study site on the left side of the TC track (fig. S4). Thus, it appears unlikely that cooling on the opposite side of the island was sufficient to counteract the air-sea enthalpy fluxes we estimated for the sites on the southern coastline. We emphasize that, although the anomalously elevated SSTs were a large-scale phenomenon, the processes governing these patterns are varying and complex. The baroclinic dynamics we have reported here that maintained the elevated SSTs over the insular shelf, shelf break, and upper slope of our study area represent a previously unidentified mechanism by which the upper ocean can affect TC heat fluxes, but it is one process among many contributing to the storm's overall energetics.

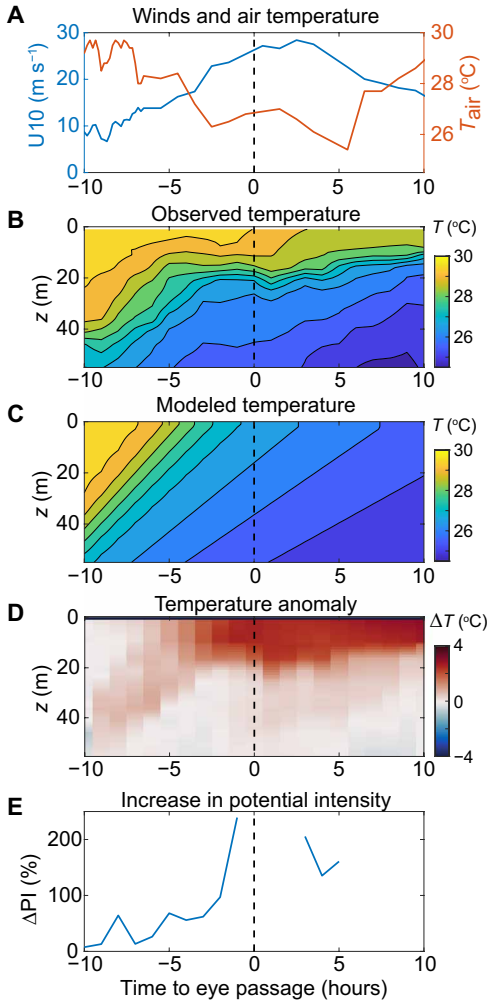

Fig. 4. Effect of elevated SSTs on hurricane PI. (**A**) Wind speed at 10-m above the ocean surface (U10, blue) and air temperature (T_{air}, orange) from buoy 42085. (**B**) Observed hourly averaged water column temperature (T_{obs}) from the upper slope. (**C**) Modeled hourly temperature (T_{mod}) with no shelf-break impedance of shoaling isotherms. (**D**) Temperature anomaly resulting from the observed conditions ($\Delta T = T_{obs} - T_{mod}$). (**E**) Percent reduction in potential intensity (PI) from the modeled SSTs compared to the observed. The vertical dashed line in each panel indicates the time of eye passage.

New framework of TC dynamics near steep island coasts

These results present a new framework for understanding how a stratified ocean may respond to TC forcing along steep coastal margins. Previous work has found three predominant coastal ocean baroclinic responses to TC winds during the initial forced stage: (i) cooling from shear-induced mixing (*14*, *15*), (ii) restricted cooling due to downwelling and offshore advection of cold bottom water (*16*), and (iii) warming due to downwelling circulation and suppression of upwelling (*20*, *21*). Our observations document a previously unidentified response, whereby offshore-directed TC winds along a relatively narrow insular shelf with a steep slope result in sustained, warm SSTs throughout the storm, despite the influx of increasingly cold waters at depth. These subsurface dynamics are generally not observable by surface observation platforms, such as buoys or remote sensing methods. A simplified cross-shelf schematic shows how the direction of TC forcing in relation to the coastline effectively stabilized the water column structure and suppressed turbulence and mixing in the upper ocean until the impact of the cold trailing wake (Fig. 5).

Our direct observations of TC coastal dynamics are particularly pertinent to thousands of small islands in the global ocean with similarly narrow insular shelves and steep slopes. The circuitous nature of island margins allows portions of the coastline to experience offshore-directed winds during the TC approach more so than broad continental landmasses. While Atlantic continental TC research continues to advance, much less is understood about TC interactions with small islands (*39*), whose communities are especially vulnerable to TC impacts due to their relative isolation, and the increased mortality and injury burden to populations with less developed infrastructure and access to resources (*40*, *41*). In addition, the destructiveness of TCs is projected to increase with climate change not only due to sea-level rise and increased flooding (*42*) but also because the storm life spans, intensities, and intensification rates are projected to increase with warming SSTs (*43*–*46*), particularly

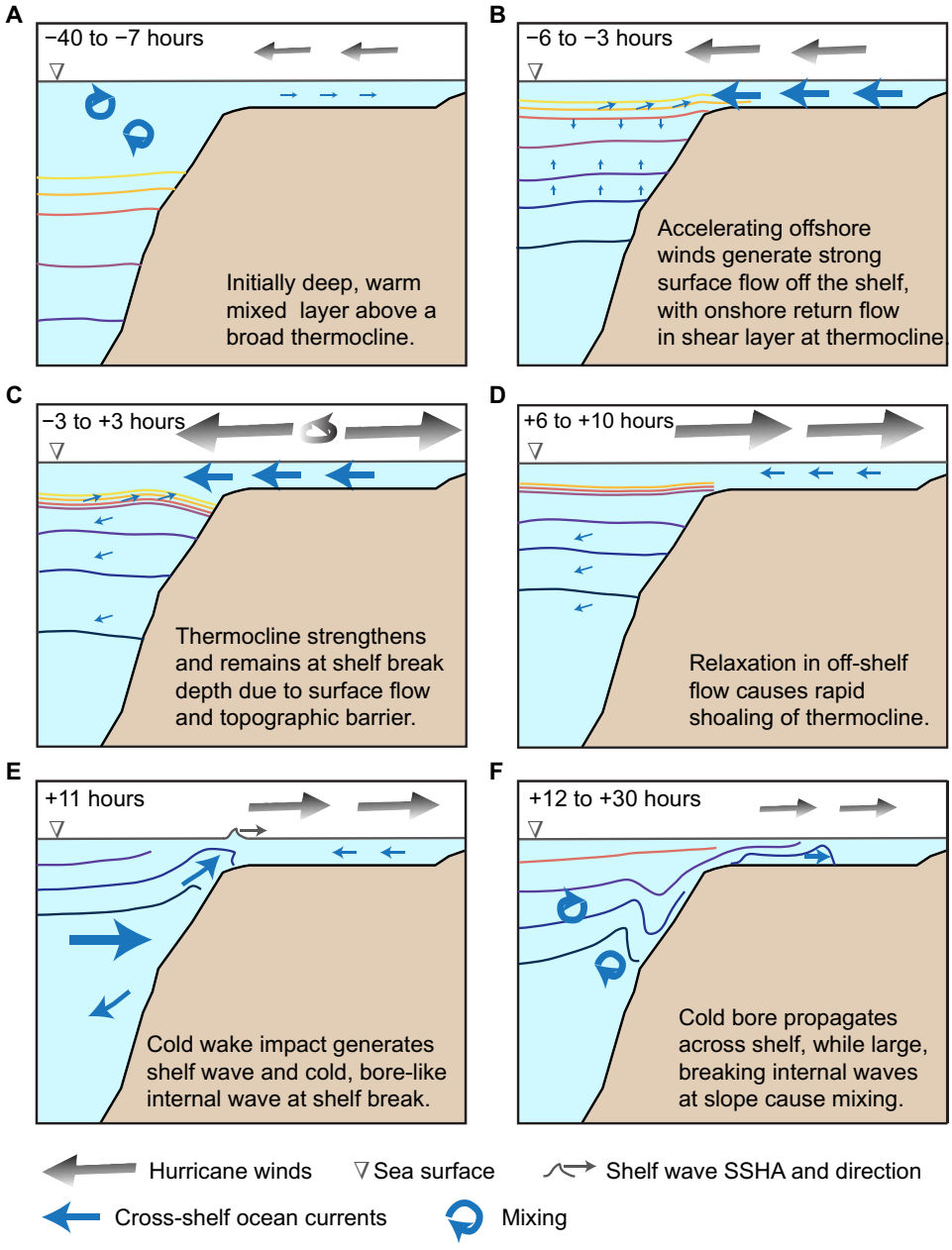

Fig. 5. Schematic representation of cross-shore baroclinic dynamics during the passage of Hurricane María. Times in the top left of each panel are relative to the eye passage. Size and direction of gray arrows indicate magnitude and heading of winds relative to the cross-shore profile, and blue arrows represent cross-shore and vertical current velocities. (**A**) With the approach of María, the thermocline was initially deep and broad over the upper slope. (**B**) As off-shelf winds accelerated, an off-shelf surface flow developed, isotherms shoaled and compressed, and stratification increased. (**C**) During the eye passage, the off-shelf surface flow strengthened, arresting the upward movement of the thermocline at the shelf break, which allowed the persistence of elevated SSTs during the storm. (**D**) Hours after the wind reversal, the surface flow relaxed and the thermocline shoaled rapidly. (**E**) Approximately 11 hours after the eye passage, the trailing cold wake affected the upper slope, generating a topographic shelf wave with an SSHA peak (gray surface wave) and a cold, bore-like internal wave at depth. (**F**) The surface shelf wave peak and the cold bore propagated across the shelf, while the reverberation of the wake against the steep, upper slope caused large, breaking internal waves.

for the Atlantic (*47*, *48*) and Western Pacific ocean basins (*33*) where thousands of small islands are found.

Limitations of empirical data

Although our high-resolution measurements have revealed energetic, high-frequency baroclinic dynamics induced by TC forcing, they are limited by our lack of spatial coverage and perspective on alongshore processes. These observations serve to underscore the present dearth in our collective understanding of how extreme storms such as TCs interact with and evolve in proximity to insular island margins. Additional in situ observations would be helpful, but these mostly arise from accidental capture of TC events. Therefore, the development of very high resolution, coupled, air-sea models is a necessary tool for exploring the sensitivity of TC intensity to these

observed coastal processes and provides a promising avenue for ensuring that scientific efforts can benefit island communities and nations in the face of increasingly severe TCs.

MATERIALS AND METHODS

Experimental design

The study area was off the southwest coast of Puerto Rico (Fig. 1), and water column observations were taken from a slope site, a shelf break site, and an outer shelf site, with an additional array of six nearshore sites.

Slope site

Technical scuba divers deployed a benthic instrument package at a 55-m site on the upper insular slope, which was established by the University of Puerto Rico–Mayagüez's multidisciplinary Mesophotic Coral Ecosystem research program (*27*); the slope here faces south-southwestward and is steep (~44°). An upward-looking 300-kHz Teledyne RD Instruments acoustic Doppler current profiler collected current velocity profiles of horizontal and vertical velocities in 1-m bins from 4 to 49 m above the bed (mab); these profiles were averages of 60 samples taken at 2 Hz, resulting in an expected SD of 1.6 cm s^{-1} for horizontal velocities, and no more than 0.8 cm s^{-1} for vertical velocities (Teledyne RDI communications). A SeaBird Electronics SBE-37 temperature-salinity (TS) sensor was sampled once every 2 min and was mounted at 0.2 mab. A subsurface mooring was deployed approximately 15 m (horizontally) further downslope from the benthic instrument package at 62-m water depth. The mooring consisted of one SeaBird SBE-56 thermistor at 57-m depth that logged every 30 s and eight RBR SoloT thermistors mounted every 5 m from 52-m to 17-m depth that sampled every 5 s; a SeaBird Electronics SBE-37 TS sensor that sampled once every 2 min was at the top of the mooring at a depth of 12 m.

Shelf break site

A second mooring was deployed at the insular shelf break, directly onshore (181 m horizontal distance away) from the slope site, at 18-m water depth. This mooring had three thermistors all sampling at 30 s: an SBE-56 thermistor at 18-m depth (0.2 mab) and two RBR thermistors at 14- and 9-m depth (4 and 9 mab). An RBR Virtuoso pressure gauge installed at 18-m depth (0.2 mab) collected hourly bursts of 4096 samples at 4 Hz (~17 min). The pressure data were averaged across bursts, and the atmospheric pressure was removed (using buoy record, see below).

Outer shelf site

A benthic instrument package was deployed at 12-m depth on the outer insular shelf ~12 km east-northeast of the slope and shelf break sites. An upward-looking 600-kHz Nortek acoustic wave and current (AWAC) profiler measured directional waves with hourly burst of 2048 pressure and acoustic surface tracking (AST) samples at 1 Hz. The AWAC also collected a 5-min averaged profile of current velocity in 2-m bins every 10 min after the wave sampling period (at 0, 40, and 50 min each hour); temperature was also recorded with the same sampling scheme. Given the AWAC sampling parameters, the expected error in current velocity is 1.4 cm s^{-1} for horizontal currents and 0.5 cm s^{-1} for vertical currents. Because of the low pressure during Hurricane María, pressure-derived wave parameters were erroneous, so all presented wave statistics from this site are from AST.

Nearshore sites

Instrument packages installed just above the bed at six nearshore sites (P1 to P6; 10-m depth) consisted of a single-point Marotte current meter and an RBR Virtuoso pressure gauge. The Marottes recorded near-bed temperature, which was binned into hourly averages. RBRs recorded pressure with hourly bursts of 4096 samples at 4 Hz (~17 min); to obtain water levels, the pressure data were averaged across bursts and the atmospheric pressure was removed (using buoy record, see below).

Auxiliary data

Additional meteorologic and oceanographic data were obtained from two buoys of the Caribbean Integrated Coastal Ocean Observing System ("CariCOOS" buoys 42085 and 41053; www.caricoos.org/). Buoy 42085 is located approximately 40 km east of our study area, whereas buoy 41053 is located off San Juan on the northern side of the island (Fig. 1A). Best track data for Hurricane María were obtained from the National Oceanographic and Atmospheric Administration National Hurricane Center GIS archive (www.nhc.noaa.gov/gis/). To correct pressure measurements from our study sites, the atmospheric pressure data from buoy 42085 were time-adjusted relative to the eye passage. Daily satellite SST data were obtained from National Oceanic and Atmospheric Administration's (NOAA's) National Centers for Environmental Information (NCEI) Optimal Interpolation Sea Surface Temperature (OISST) v2.1 analysis (*49*).

Data analysis

Density was derived from temperature; using the temperature and density measured by the near-surface and near-bed TS sensors on the slope mooring, a linear relationship was found for each time step and applied to the water column temperature. The Brunt-Väisälä (buoyancy) frequency, N, was calculated as $N^2 = -(g/\rho_o)(\delta\rho/\delta z)$, where g is the gravitational acceleration, ρ_o is the depth-averaged density, and $\delta\rho/\delta z$ is the vertical density gradient. The gradient Richardson number, Ri_g, was computed as $Ri_g = N^2/S^2$, where S is the current shear, $S = \sqrt{(du/dz)^2 + (dv/dz)^2}$; to calculate Ri_g, N^2 was interpolated to the shear vertical resolution of 1 m. Regions with $Ri_g < 0.25$ are prone to shear instabilities (*50*), and this threshold is often invoked as requisite for turbulence. The Thorpe scale, L_T, is the root mean square of the displacement caused by adiabatically reordering the density profiles (*51*). TKE dissipation was estimated as $\varepsilon = 0.64 L_T^2 N^3$ (*52*). We note that the L_T and ε estimates rely on temperature measured at 5-m depth intervals; as such, our minimum resolvable overturn is 5 m. The internal Froude number, F_r, versus depth was calculated for the slope site using $F_r(z) = |u(z)/c(z)|$, where u is the current speed and c is the first mode phase speed, which was estimated using $c = 1/\pi \int_{-H}^{0} N(z)dz$, where H is water depth (*53*). SSHAs were calculated by de-tiding the water levels measured by the pressure sensors at the shelf break and nearshore sites.

To examine the effect of wave-induced turbulence on the mixed layer depth, we calculated the wave-amplitude Reynolds number (*28*): $Re = (\omega/\nu)\, a_0^2 \exp(-2z\omega/g)$, where ω is the wave frequency, a_0 is the wave amplitude, ν is the kinematic viscosity of ocean water, and z is the depth. Then, to determine the time period when the surface waves drove turbulence capable of deepening the mixed layer depth, the times when Re exceeded a critical value ($Re_{cr} = 3000$) were identified.

To evaluate the change in potential storm intensity that would result in the absence of the baroclinic processes at the shelf break, we compared our water column temperature to that of a modeled water column in which the upward movement of the isotherms is not impeded at the shelf break. Both the modeled and observed data

use the buoy SST (time-adjusted relative to the eye passage) and the 9-m temperature from the shelf break mooring, in addition to the water column temperature from the slope. For the modeled temperature, the initial profile is the average taken over 00:00 on 19 September to 08:00 on 20 September (the time when the isotherms begin shoaling) and the depths of the temperatures below the slope site water depth (62 m) were estimated using the isotherm shoaling rates and the timing of when these deeper isotherms appeared at the slope site. The temperature-dependent shoaling rates were then applied to this initial temperature profile in hourly increments and compared to the hourly averaged observations. Then, with the resulting observed and modeled SSTs, PI was calculated as

$$\mathrm{PI}^2 = \frac{C_k}{C_d}\frac{\mathrm{SST} - T_o}{T_o}(k_s - k_a)$$

where C_k and C_d are the enthalpy and drag exchange coefficients, respectively; k_s and k_a are the specific enthalpies of air at the ocean surface and in the ambient boundary layer; and T_o is the outflow temperature (*36*). Values of $C_k = 1.16 \times 10^{-3}$ (*54*) and $C_d = 2.4 \times 10^{-3}$ (*55*) were used, and the specific enthalpies were found using standard bulk formulae (*56*). To was obtained from the National Centers for Environmental Prediction (NCEP) Daily Global Analyses data provided by the NOAA Earth System Research Laboratory Physical Sciences Division (www.esrl.noaa.gov/psd/).

SUPPLEMENTARY MATERIALS

Supplementary material for this article is available at http://advances.sciencemag.org/cgi/content/full/7/20/eabf1552/DC1

REFERENCES AND NOTES

1. M. DeMaria, C. R. Sampson, J. A. Knaff, K. D. Musgrave, Is tropical cyclone intensity guidance improving? *Bull. Am. Meteorol. Soc.* **95**, 387–398 (2014).
2. J. Kaplan, M. DeMaria, Large-scale characteristics of rapidly intensifying tropical cyclones in the North Atlantic basin. *Weather Forecast.* **18**, 1093–1108 (2003).
3. J. Kaplan, M. DeMaria, J. A. Knaff, A revised tropical cyclone rapid intensification index for the Atlantic and Eastern North Pacific basins. *Weather Forecast.* **25**, 220–241 (2010).
4. R. Rogers, S. Aberson, A. Aksoy, B. Annane, M. Black, J. Cione, N. Dorst, J. Dunion, J. Gamache, S. Goldenberg, S. Gopalakrishnan, J. Kaplan, B. Klotz, S. Lorsolo, F. Marks, S. Murillo, M. Powell, P. Reasor, K. Sellwood, E. Uhlhorn, T. Vukicevic, J. Zhang, X. Zhang, NOAA's hurricane intensity forecasting experiment: A progress report. *Bull. Amer. Meteor. Soc.* **94**, 859–882 (2013).
5. K. Ooyama, Numerical simulation of the life-cycle of tropical cyclones. *J. Atmos. Sci.* **26**, 3–40 (1969).
6. J. F. Price, Upper ocean response to a hurricane. *J. Phys. Oceanogr.* **11**, 153–175 (1981).
7. I. Ginis, Tropical cyclone-ocean interactions, in *Atmosphere-Ocean Interactions*, W. Perrie, Ed. (WIT Press, 2002), vol. 33, pp. 83–114.
8. L. K. Shay, G. J. Goni, P. G. Black, Effects of a warm ocean feature on Hurricane Opal. *Mon. Wea. Rev.* **128**, 1366–1383 (2000).
9. J. C. L. Chan, Y. Duan, L. K. Shay, Tropical cyclone intensity change from the simple ocean-atmosphere coupled model. *J. Atmos. Sci.* **58**, 154–172 (2001).
10. E. M. Vincent, M. Langigne, J. Vialard, G. Madec, N. C. Jourdain, S. Masson, Assessing the oceanic control on the amplitude of sea surface cooling induced by tropical cyclones. *J. Geophys. Res.* **117**, C05023 (2012).
11. J. C. L. Chan, Y. Duan, L. K. Shay, Tropical cyclone intensity change from a simple ocean-atmosphere coupled model. *J. Atmos. Sci.* **58**, 154–172 (2001).
12. I. D. Lloyd, G. A. Vecchi, Observational evidence for oceanic controls on hurricane intensity. *J. Climate* **24**, 1138–1153 (2010).
13. L. Jyothi, S. Joseph, P. Suneetha, Surface and sub-surface ocean response to Tropical Cyclone Phailin: Role of pre-existing oceanic features. *J. Geophys. Res. Oceans* **124**, 6515–6530 (2019).
14. S. M. Glenn, T. N. Miles, G. N. Seroka, R. K. Forney, F. Yu, H. Roarty, O. Schofield, J. Kohut, Stratified coastal ocean interactions with tropical cyclones. *Nat. Commun.* **7**, 10887 (2016).
15. G. Seroka, T. Miles, Y. Xu, J. Kohut, O. Schofield, S. Glenn, Rapid shelf-wide cooling response of a stratified coastal ocean to hurricanes. *J. Geophys. Res. Oceans* **122**, 4845–4867 (2017).
16. T. Miles, G. Seroka, S. Glenn, Coastal ocean circulation during Hurricane Sandy. *J. Geophys. Res. Oceans* **122**, 7095–7114 (2017).
17. D. A. Mitchell, W. J. Teague, E. Jarosz, W. Wang, Observed currents over the outer continental shelf during Hurricane Ivan. *Geophys. Res. Lett.* **32**, L11610 (2005).
18. W. J. Teague, E. Jarosz, D. W. Wang, D. A. Mitchell, Observed oceanic response over the upper continental slope and outer shelf during Hurricane Ivan. *J. Phys. Oceanogr.* **37**, 2181–2206 (2007).
19. H. Potter, S. F. DiMarco, A. H. Knap, Tropical cyclone heat potential and the rapid intensification of Hurricane Harvey in the Texas Bight. *J. Geophys. Res. Oceans* **124**, 2440–2451 (2019).
20. Z. Zhang, Y. Wang, W. Zhang, J. Xu, Coastal ocean response and its feedback to Typhoon Hato (2017) over the South China Sea: A numerical study. *J. Geophys. Res. Atmos.* **124**, 13731–13749 (2019).
21. B. Dzwonkowski, J. Coogan, S. Fournier, G. Lockridge, K. Park, T. Lee, Compounding impact of severe weather events fuels marine heatwave in the coastal ocean. *Nat. Commun.* **11**, 4623 (2020).
22. K. Nadaoka, Y. Nihei, R. Kumano, T. Yokobori, T. Omija, K. Wakaki, A field observation on hydrodynamic and thermal environments of a fringing reef at Ishigaki Island under typhoon and normal atmospheric conditions. *Coral Reefs* **20**, 387–398 (2001).
23. T. A. Schramek, E. J. Terrill, P. L. Colin, B. D. Cornuelle, Coastally trapped waves around Palau. *Cont. Shelf Res.* **191**, 104002 (2019).
24. C. Santos-Burgoa, A. Goldman, E. Andrade, N. Barrett, U. Colon-Ramos, M. Edberg, S. Zeger, Ascertainment of the estimated excess mortality from Hurricane Maria in Puerto Rico (Project Report, Milkin Institute School of Public Health, George Washington University, 2018).
25. NHC, Costliest U.S. tropical cyclones tables updated (National Oceanic and Atmospheric Administration National Hurricane Center, NOAA Technical Memorandum NWS NHC-6, 2018); https://nhc.noaa.gov/dcmi.shtml.
26. T. Houser, P. Marsters, The world's second largest blackout (Rhodium Group Report, 2018); https://rhg.com/research/puerto-rico-hurricane-maria-worlds-second-largest-blackout/.
27. C. Sherman, M. Nemeth, H. Ruíz, I. Bejarano, R. Appledoorn, F. Pagán, M. Schärer, E. Weil, Geomorphology and benthic cover of mesophotic coral ecosystems of the upper insular slope of southwest Puerto Rico. *Coral Reefs* **29**, 347–360 (2010).
28. A. V. Babanin, On a wave-induced turbulence and a wave-mixed upper ocean layer. *Geophys. Res. Lett.* **33**, L20605 (2006).
29. A. Toffoli, J. McConochie, M. Ghantous, L. Loffredo, A. V. Babanin, The effect of wave-induced turbulence on the ocean mixed layer during tropical cyclones: Field observations on the Australian North-West Shelf. *J. Geophys. Res.* **117**, C00J24 (2012).
30. J. E. Geisler, Linear theory of the response of a two-layer ocean to a moving hurricane. *Geophys. Fluid Dyn.* **1**, 249–272 (1970).
31. T. M. S. Johnston, S. Wang, C.-Y. Lee, J. N. Moum, D. L. Rudnick, A. Sobel, Near-inertial wave propagation in the wake of Super Typhoon Mangkhut: Measurements from a profiling float array. *J. Geophys. Res.* **126**, e2020JC016749 (2021).
32. A. E. Yanokvksy, Large-scale edge waves generated by hurricane landfall. *J. Geophys. Res.* **114**, C03014 (2009).
33. Q. Ji, F. Xu, J. Xu, M. Liang, S. Tu, S. Chen, Large-scale characteristics of landfalling tropical cyclones with abrupt intensity change. *Frontiers Earth Sci.* **13**, 808–816 (2019).
34. R. J. Pasch, A. B. Penny, R. Berg, National hurricane center tropical cyclone report—Hurricane Maria (NOAA, al152017, 2018).
35. A. T. Hazelton, M. Bender, M. Morin, L. Harris, S.-J. Lin, 2017 Atlantic hurricane forecasts from a high-resolution version of the GFDL fvGFS model: Evaluation of track, intensity, and structure. *Weather Forecast.* **33**, 1317–1337 (2018).
36. K. A. Emanuel, Thermodynamic control of hurricane intensity. *Nature* **401**, 665–669 (1999).
37. Y. Miyamoto, T. Takemi, An effective radius of the sea surface enthalpy flux for the maintenance of a tropical cyclone. *Atmos. Sci. Lett.* **11**, 278–282 (2010).
38. Y. Wang, J. Xu, Energy production, frictional dissipation, and maximum intensity of a numerically simulated tropical cyclone. *J. Atmos. Sci.* **67**, 97–116 (2010).
39. T. E. Marler, Pacific island tropical cyclones are more frequent and globally relevant, yet less studied. *Front. Environ. Sci.* **2**, 42 (2014).
40. S. Doocy, A. Dick, A. Daniels, T. D. Kirsch, The human impact of tropical cyclones: A historical review of events 1980-2009 and systematic literature review. *PLOS Curr.* **5**, ecurrents.dis.2664354a5571512063ed29d25ffbce74 (2013).
41. R. A. Pielke Jr., J. Rubiera, C. Landsea, M. L. Fernández, R. Klein, Hurricane vulnerability in Latin America and the Caribbean: Normalized damage and loss potentials. *Nat. Hazards Rev.* **4**, 101–114 (2003).
42. J. D. Woodruff, J. L. Irish, S. J. Camargo, Coastal flooding by tropical cyclones and sea-level rise. *Nature* **504**, 44–52 (2013).
43. K. Emanuel, Increasing destructiveness of tropical cyclones over the past 30 years. *Nature* **436**, 686–688 (2005).

44. W. Mei, S.-P. Xie, F. Primeau, J. C. McWilliams, C. Pasquero, Northwestern Pacific typhoon intensity controlled by changes in ocean temperature. *Sci. Adv.* **1**, e1500014 (2015).
45. K. T. Bhatia, G. A. Vecchi, T. R. Knutson, H. Murakami, J. Kossin, K. W. Dixon, C. E. Whitlock, Recent increases in tropical cyclone intensification rates. *Nat. Commun.* **10**, 635 (2019).
46. J.-E. Chu, S.-S. Lee, A. Timmermann, C. Wengel, M. F. Stuecker, R. Yamaguchi, Reduced tropical cyclone densities and ocean effects due to anthropogenic greenhouse warming. *Sci. Adv.* **6**, eabd5109 (2020).
47. K. Balaguru, G. R. Foltz, L. R. Leung, Increasing magnitude of hurricane rapid intensification in the Central and Eastern Tropical Atlantic. *Geophys. Res. Lett.* **45**, 4238–4247 (2018).
48. T. R. Knutson, J. L. McBride, J. Chan, K. Emanuel, G. Holland, C. Landsea, I. Held, J. P. Kossin, A. K. Srivastava, M. Sugi, Tropical cyclones and climate change. *Nat. Geosci.* **3**, 157–163 (2010).
49. V. Banzon, T. M. Smith, T. M. Chin, C. Liu, W. Hankins, A long-term record of blended satellite and in situ sea-surface temperature for climate monitoring, modeling and environmental studies. *Earth Syst. Sci. Data* **8**, 165–176 (2016).
50. J. W. Miles, On the stability of heterogenous shear flows. *J. Fluid Mech.* **10**, 496–508 (1961).
51. S. A. Thorpe, Turbulence and mixing in a Scottish loch. *Philos. Trans. R. Soc. A* **286**, 125–181 (1977).
52. T. M. Dillon, Vertical overturns: A comparison of Thorpe and Ozmidov length scales. *J. Geophys. Res.* **87**, 9601–9613 (1982).
53. D. B. Chelton, R. A. deSzoeke, M. G. Schlax, K. E. Naggar, N. Siwertz, Geographic variability of the first baroclinic Rossby radius of deformation. *J. Phys. Oceanogr.* **28**, 433–460 (1998).
54. J. A. Zhang, P. G. Black, J. R. French, W. M. Drennan, First direct measurements of enthalpy flux in the hurricane boundary layer: The CBLAST results. *Geophys. Res. Lett.* **35**, L14813 (2008).
55. M. A. Donelan, B. K. Haus, N. Reul, W. J. Plant, M. Stiassnie, H. C. Graber, O. B. Brown, E. S. Saltzman, On the limiting aerodynamic roughness of the ocean in very strong winds. *Geophys. Res. Lett.* **31**, L18306 (2004).
56. M. Holmgren, X Steam, Thermodynamic properties of water and steam, MATLAB Central File Exchange (2019); https://www.mathworks.com/matlabcentral/fileexchange/9817-x-steam-thermodynamic-properties-of-water-and-steam.

Acknowledgments: We thank J. Logan, C. Johnson, and M. Buckley [U.S. Geological Survey (USGS)] and M. Carlo, H. Xu, and E. Tuohy (UPR-M) for their help with field work and data collection. We gratefully acknowledge M. C. Silander (UPR-M) for providing the San Juan buoy data. We also thank J. Warrick (USGS) for an initial review of the manuscript and E. McPhee-Shaw (UWW), M. McManus (UH), S. Vitousek (USGS), and M. Lindhart (Stanford) for helpful discussions. Any use of trade, firm, or product names is for descriptive purposes only and does not imply endorsement by the U.S. government. **Funding:** This work was funded by the USGS's Coastal and Marine Hazards and Resources Program via the USGS Coral Reef Project. Partial funding was also provided by National Science Foundation OCE Award No. 1809878.
Author contributions: O.M.C. synthesized and analyzed the multiple data sets and wrote the manuscript in collaboration with C.D.S. C.D.S. and C.E.S. designed the field study, which was performed in conjunction with the other authors. K.J.R. was involved in data collection and processing. W.E.S. assisted with the shelf-break measurements. All authors reviewed and edited this manuscript. **Competing interests:** The authors declare that they have no competing interests. **Data and materials availability:** Data used in this study are available at https://doi.org/10.5066/P9IXOHID, except for the auxiliary datasets, which are available via websites given in Materials and Methods.

Submitted 7 October 2020
Accepted 24 March 2021
Published 12 May 2021
10.1126/sciadv.abf1552

Citation: O. M. Cheriton, C. D. Storlazzi, K. J. Rosenberger, C. E. Sherman, W. E. Schmidt, Rapid observations of ocean dynamics and stratification along a steep island coast during Hurricane María. *Sci. Adv.* **7**, eabf1552 (2021).